Hematite Photoelectrodes Grown on Porous CuO-Sb_2O_5-SnO_2 Ceramics for Photoelectrochemical Water Splitting

Alexander N. Bondarchuk [a]*, Iván Corrales-Mendoza [a], Frank Marken [c], Luis Á. Arellanes-Mendoza [a], Josué A. Aguilar-Martínez [b], L.G. Silva-Vidaurri[d], Gonzalo Curiel-Olivares [a], F. Montejo-Alvaro[a]

[a] Universidad Tecnológica de la Mixteca, Huajuapan 69000, Oaxaca, México

[b] Facultad de Ingeniería Mecánica y Eléctrica, Centro de Investigación e Innovación en Ingeniería Aeronáutica, Universidad Autónoma de Nuevo León, Carretera a Salinas Victoria km. 2.3, C.P. 66600 Apodaca, Nuevo León, México

[c] Department of Chemistry, University of Bath, Claverton Down, Bath BA2 7AY, UK

[d] Centro de Investigación en Materiales Avanzados, S.C., Unidad Monterrey Parque PIIT, Nueva Carretera al Aeropuerto Km 10 CP. 66600, Apodaca, N.L., México.

Keywords: Hematite, Tin-dioxide ceramics, Photoanode, Water splitting, Solar energy

Abstract

Photoelectrodes capable of cost-effective hydrogen production on a large scale, via photoelectrochemical water splitting under solar light, could offer an elegant solution to many current problems of humankind caused by over-reliance on fossil fuels and the resulting environmental pollution. The search and design of low-cost photoelectrode materials and substrates for practical applications are required. In this work, unmodified hematite photoanodes grown by metal-organic chemical vapor deposition (MO-CVD) onto CuO-Sb_2O_5-SnO_2 ceramic substrates are reported. The deposition time of hematite precursor varied between 10 min, 60 min, and 90 min. The photoanode grown for 60 min exhibits the highest photocurrent density recorded at 1.23 V vs RHE (reversible hydrogen electrode): 4.79 mA/cm^2 under blue light of Thorlabs LED M455L2 (455 nm), 0.41 mA/cm^2 under the radiation of the real sun in Mexico, and 0.38 mA/cm^2 under AM1.5G solar simulator conditions. The high porosity of CuO-Sb_2O_5-SnO_2 ceramics permits the permeation of the hematite precursor into the substrate bulk, which results in 3D-growth of a thin Fe_2O_3-coating (50 nm or less) on conductive SnO_2-grains in the ceramics to a depth of ca. 5 µm. The thick photocatalytic layer (SnO_2-grains coated by hematite) of several micrometers assures a good light harvesting by the photoelectrode, while the nano-sized Fe_2O_3-films on conductive SnO_2-grains is favorable for charge diffusion. This architecture of the photoelectrode results in good photoelectrochemical characteristics and is promising for further development.

1. Introduction

The depletion of fossil fuels, global warming, and environmental pollution make the shift away from fossil-based energy sources towards environmentally friendly and renewable ones inevitable. In this context, the development of solar energy technologies is a very attractive path to resolve the current problems of humankind and to satisfy future energy needs [1-7].

The direct harvesting of solar energy, its conversion, and storage in the form of hydrogen fuel can be realized via photoelectrochemical (PEC) water splitting. During this process, water molecules on the surface of photo-active materials under solar light dissociate into oxygen (at the photoanode) and hydrogen (at the photocathode), the latter of which can be used as high-energy and environmentally friendly fuel. However, to date, the practical application of this technology to produce hydrogen is hindered for a number of reasons mentioned hereafter. To achieve high performance in PEC water splitting, the active photoelectrode material should meet a number of special requirements, such as high stability in an aqueous environment, strong light absorption in the visible region of the spectrum of solar radiation, a suitable band edge position for reduction/oxidation of water, and a solar-to-hydrogen (STH) efficiency of 10% or higher [1-3, 8-11]. In addition, the photoelectrode cost should be relatively low for large-scale production. This means the restriction in using noble metal catalysts (like platinum, gold or iridium), as well as a limitation in the application of complicated production technologies that need expensive equipment. To date, photoelectrodes meeting all these requirements and having a low cost for large scale manufacturing for example on low cost ceramic substrates, have not been developed to the best of our knowledge.

According to the literature [1-21], hematite (α-Fe_2O_3) is one of the most promising photocatalytic materials for photo-anode applications. Particularly pioneering contributions by Grätzel and coworkers have progressed this field [22-24]. For the hematite photoelectrode, the theoretical maximum photocurrent density is ca. 12 mA cm^{-2} (for nano-structured interfaces) at 1.23 V versus RHE, which corresponds to the STH efficiency of 15% under AM 1.5 solar spectral illumination [25]. However, the highest photocurrent density which has been reported to date for hematite photoelectrodes was only 4.68 mA cm^2 at 1.23 V vs. RHE under the standard AM1.5G solar light illumination [26]. This photoelectrode was synthesized via the electrochemical method and modified with Ag nanoparticles and Co–Pi cocatalyst. For the unmodified photo-anode of pristine hematite, the photocurrent registered at 1.23 V vs. RHE does not usually exceed 1 mA cm^{-2} under one sun illumination [27-34]. This suggests that the potential of this material has not been exploited fully at the present time, and the higher PEC performance of α-Fe_2O_3 photoelectrode can be achieved.

One of the approaches to improve the PEC performance of photoelectrodes can be the engineering of the conductive substrate and/or its optimization under certain photoactive material [18-20]. For example, the photoelectrodes fabricated according to the so-called “host-guest” strategy [35-41] involve the engineering of the conductive substrate aiming to increase their active surface area and to improve electron collection. This is usually reached by forming the hierarchical structure of electrodes when one layer or multilayers of photocatalytic material (“guest”) are deposited on the substrate (“host”) with a high surface area. In this case, the photoactive material can be deposited on the surface by thin layers that are favorable for hole diffusion, while a good light harvesting and the electron collection are assured by 3D relief of conductive substrate and by multilayers of the photocatalytic coating. To date, such substrates have been obtained, for example, as: thin mesoporous SiO_2 host template coated with a

conductive thin layer of TiO_2 to support the α-Fe_2O_3 film [36]; highly porous SnO_2 nanosheet arrays sandwiched within TiO_2 and CdS quantum dots [37]; 3D porous niobium doped tin oxide electrodes fabricated by atomic layer deposition [38]; self-assembled 6 nm nanocrystalline Sb-doped SnO_2 spheres onto glass during a multi-step coating procedure [39]. The approach of "host-guest" strategy was implemented, for example, in the fabrication of gold nanorod substrate which was grown inside the aluminum oxide membrane to provide a conductive and nanostructured surface acting as the current collector [41]. The hematite photoelectrode grown on this Au-substrate showed a record high value of photocurrent, about 8 mA/cm^2 (at 0.6 V vs. Ag/AgCl) under 1 sun illumination. However, such technologies to form 3D-structured substrate involved relatively complicated fabrication procedures and/or the utilization of expensive materials, such as Pt or Au. This hinders the application of such substrates in large-scale production of photoelectrodes which requires more simple and low-cost technologies.

Recently, we reported conductive and porous SnO_2-Sb_2O_5 ceramics as a promising candidate to be used as substrates ("host") for photocatalytic coating of hematite [42] and bismuth vanadate [43]. It is worth mentioning here that tin dioxide is widely used to prepare different optoelectronic devices and composite materials, for example, perovskite solar cells [44-47], varistors [48-50], gas sensors [51-53]. For the photoelectrodes prepared in [42], the hematite coating was grown by the aerosol-assisted chemical vapor deposition (AA-CVD). SnO_2-Sb_2O_5 ceramics applied as a substrate have been sintered at relatively high temperature (1300°C), which assures good electric contacts between grains and opens a possibility of additional heat treatment of photoelectrode at high temperature. The porosity of ceramics permits the growth of the photoactive layer (SnO_2-grains covered by photocatalytic material), not only at surface of the substrate, but also within it at depth. The conductive nano- and macro-grains form an electrical path for electrons through the ceramic substrate that assures their collection. Tin dioxide is transparent for visible solar light (360-740 nm) due to its wide bandgap (about 3.6 eV [34]). This suggests that the near-surface layer of the SnO_2 substrate can be transparent for visible radiation. In this case, the photocatalytic coating formed in the substrate volume is active and makes its contribution to the photocurrent. The unmodified hematite and bismuth vanadate photoelectrodes grown on these substrates exhibit a relatively high photocurrent, 2.8 and 1.1 mA/cm^2 respectively at 1.23 V vs. RHE under blue light of Thorlabs M455L2 LED [42,43].

In the present work, the improved hematite photoelectrodes grown by the MO-CVD-technique on porous and conductive Sb_2O_5-SnO_2 ceramics modified by CuO are reported. The addition of CuO to the substrate was observed to improve performance and is not studied in any detail here. This report examines the hematite coatings as photo-active component. The photocurrent density of obtained photoelectrodes reaches about 4.79 mA/cm^2 at 1.23 V vs. RHE under blue light of Thorlabs M455L2 LED (455 nm, 198 mW cm^{-2}) or 0.38 mA/cm^2 under the AM1.5G solar simulator conditions. The incident photon-to-current efficiency is 6.59% at the wavelength of 455 nm. The reported results are discussed based on the data of scanning electron microscopy (SEM), energy-dispersive X-ray spectroscopy (EDS), X-ray diffraction (XRD), and photoelectrochemical measurements under the AM1.5G- and the sun-radiation.

2. Material and methods

Ceramic substrates to host hematite coating had a form of circular discs (9 mm in diameter and 3 mm in thickness) and were prepared from CuO-Sb_2O_5- SnO_2 ceramics sintered in the furnace CTF 17/300 in air by heating up to 1300°C followed by cooling down to room temperature. The rate of heating and cooling was 5 degrees/min. The initial oxides — SnO_2 (99 mol %), Sb_2O_5 (1 mol %), and CuO (0.2 mol %)— had purity not less than 99.5 % and were purchased from Sigma-Aldrich.

These oxides were mixed, dried and pressed into discs before sintering in the furnace as described in [39,40]. The density of sintered material was estimated by the Archimedes method [42].

The hematite coatings were grown on SnO_2 ceramics substrates by the metal-organic chemical vapor deposition technique at 380 °C [54]. The deposition time was varied for different samples and was in the range of 10-90 min. The metalorganic precursor source was Iron(III) 2,4-pentanedionate purchased from Sigma-Aldrich. The crucible-container was tuned at the temperature of 159 °C. The vaporized precursor was transferred into a horizontal cold-wall CVD chamber by employing air as carrier gas at flow rate 1.3 L/min. The basal pressure inside the chamber was kept at 17 torrs. Subsequently, the resulting samples were annealed in a Thermolyne furnace in air at 550 °C for 1 h. The rate of heating and cooling was 5°C/min. The geometric surface area of the prepared hematite photoanode was 1.13 cm^2. The Ag-electrodes to connect the photoelectrode to the external electrical circuit were formed on samples as described in [42,43].

Electrochemical measurements were performed with an Autolab PGSTAT204 potentiostat coupled with the FRA32M module which was controlled by software Nova 2.1.4. The standard three-electrode configuration (the hematite photoanode as the working electrode, a Pt-wire as the counter electrode, and a Radiometer REF201 reference electrode with a saturated KCl reference system) was used. The electrolyte solution (pH = 12.65) was 0.1 M NaOH in demineralized water. Potentials versus standard hydrogen electrode (SHE) and reversible hydrogen electrode (RHE) were recalculated from the equation (1) given in the user manual for REF201 and from the Nernst equation (2):

$$E_{SHE} = E_{Ag/AgCl} + 0.199\ V \quad (1)$$

$$E_{RHE} = E_{Ag/AgCl} + 0.0591 \times pH + 0.1976\ V \quad (2)$$

The blue LED (455 nm, Thorlabs M455L2) with the light chopping frequency of 0.03Hz was used as a source of light. Its emitting radiation (198 mW cm^{-2} at the wavelength of 455 nm) was estimated by the laser-power meter OPHIR with a PD200W-SH head. In addition, the photoelectrodes were tested under the radiation of the solar simulator PICO G2V (AM1.5G) with a spectral bandwidth of 350nm – 1100nm (79.1 mW/cm^2) and of the Sun in Mexico (17°48'14"N 97°46'33"O) at 12am., March 23rd, 2020. The incident photon-to-current efficiency (IPCE) was calculated from the following equation [55]:

$$IPCE(\lambda) = IJ_{ph}(mA/cm^2)I \times 1239.8\ (V{\times}nm) / [P_{light}(mW/cm^2) \times \lambda(nm)], \quad (3)$$

where J_{ph} - is the photocurrent density registered under radiation with the wavelength λ and the intensity P_{light}.

Electrochemical impedance spectra (EIS) were registered by the Autolab unit in the frequency range from 0.01 Hz to 1 kHz using the ac signal with an amplitude of 10 mV at the fixed DC voltage of 1 V vs. RHE. In this experiment, the photoelectrode was irradiated by the blue light of the LED Thorlabs M455L2. Impedance data analysis was performed with Zview software (Scribner, US) with an equivalent circuit based on a Bisquert#3 transition line element with a resistor in series.

To evaluate the morphology of the materials, scanning electron microscopy (SEM, TESCAN Vega 3) coupled with the Bruker detector for energy-dispersive X-ray spectroscopy (EDS) were used. The X-ray diffraction (XRD) patterns were recorded by a PANalytical Empyrean diffractometer (CuKα radiation with λ = 1.5406 Å) operated at 45 kV and 40 mA with a Pixel detector in Bragg-Brentano geometry. The scans were performed in the 2θ range from 10 to 100° with a scan step of 0.016° and 10 s per step in continuous mode. In addition, the XRD pattern for the photoelectrode grown for 10 min was recorded as well for the second time using the grazing incidence mode at an angle of incidence 0.1°, in the range of 2θ from 20 to 90° with a scan step of 0.02° and 1 s per step. The identification of the crystalline phases was performed by applying the Inorganic Crystal Structure Database (ICSD).

Surface chemical analysis of the materials was performed by X-ray photoelectron spectroscopy (XPS) using an Escalab 250Xi Thermo Scientific K-Alpha system equipped with a monochromated AlKα X-ray source. All signals were calibrated using the C 1s peak at 284.8 eV identified with the adventitious hydrocarbon present on the sample surface. For these measurements, an energy step size of 0.1 eV, a pass energy of 20 eV, and a spot size of 650 µm were used. Prior to the XPS analysis, the samples were introduced into the load lock and degassed to pressures close to 1×10^{-8} mbar for 12 h. Subsequently, the materials were inserted into the analysis chamber where measurements were taken at a residual pressure of ca. 8×10^{-9} mbar.

3. Results and discussion

Morphology and structure

The XRD patterns for bare CuO-Sb_2O_5-SnO_2 ceramics applied as a substrate to grow the hematite photoelectrodes are shown in Fig. 1a. In this material, the presence of the tetragonal SnO_2 phase is detected only (Fig. 1a). The Cu- and Sb-phases have not been found because of low concentrations of CuO- and Sb_2O_5-additions (0.2 mol% and 1 mol% correspondently), which are below the detection limit of the diffractometer.

The XRD analysis of ceramics with photocatalytic coating grown at 10 min precursor deposition does not reveal any Fe-phases, despite the clear visual observation of a bright red layer typical for hematite on a ceramic substrate (inset in Fig. 1b). For this photoelectrode, only the tetragonal SnO_2 phase relating to the substrate is detected. A repeat study in the grazing incidence mode has not discovered any additional phases in this photoelectrode as well (Fig. 1b). The probable reason for this will be discussed below. However, for the photoelectrodes grown at 60 min and 90 min precursor deposition, Fe_2O_3 in the rhombohedral phase and SnO_2 in the tetragonal phase are found (Fig. 1c and Fig. 1d).

The SEM micrographs of bare CuO-Sb_2O_5-SnO_2 ceramics are presented in Fig. 2a. The bare CuO-Sb_2O_5-SnO_2 ceramics have a density of 6.27 g/cm^3, possess small grains with sizes in the range 200-900 nm, and are highly porous. The average pore size is about 100 nm but in some places can reach almost 1 µm. The SEM micrographs of surfaces of the hematite photoelectrodes grown at different deposition time are shown in Fig. 2b-2d. For the photoelectrodes grown at precursor deposition for 10 min (Fig. 2b), the grains with hematite coating have almost the same sizes as in bare ceramics (Fig. 2a). This suggests that the thickness of hematite coating on individual grains is very thin, about several nanometers.

For the thin film of hematite precursor, a few nm in thickness, the crystallization of Fe-phases can be hindered and so some part of iron oxide can remain in the amorphous state. This reason and a low quantity of Fe_2O_3 can be responsible for why Fe_2O_3 phases have not been detected by XRD-analysis of the photoelectrode grown for 10 min (Fig. 1b) despite this photoelectrode has the red-color coating, which is clearly visible on the substrate surface (inset in Fig. 1b) and is typical for hematite.

For photoelectrodes grown at larger deposition time (60 min or 90 min), the difference in sizes between grains of bare ceramics (Fig. 2a) and ones covered by hematite (Fig. 2c or Fig. 2d) is more notable. For the hematite photoelectrode grown for 90 min, the smallest grains have a size of about 300 nm (Fig. 2d), while ones in bare ceramics are only about 200 nm (Fig. 2a). This leads to the conclusion that the thickness of hematite film on individual SnO_2 grain can be near 50 nm for this photoelectrode. For the case of the hematite photoelectrode grown for 60 min (Fig. 2c), the Fe_2O_3 layer on individual grain can be ever thinner.

The EDS data for hematite photoelectrode grown at 60 min precursor deposition are presented in Fig. 3. The elemental map of Fe- and C- distribution shows non-uniformity of hematite coating on the photoelectrode surface (Fig. 3b). This can be seen as well from the estimation of Fe-atomic concentration made for different locations in the studied area (Fig. 3b). Moreover, as can be seen in the increased image of the individual grain in Fig.3b, hematite coating can be non-uniform on surfaces of the individual SnO_2 grain as well. In addition, there are surface areas on some individual grains which are covered by carbon more strongly than by hematite (Fig. 3a). This suggests that the thickness of the hematite coating differs in the distinct points of the same photoelectrode. These photoelectrode features probably result from 3D-relief and porosity of ceramic substrate leading to non-uniform precursor flow and distribution above its surface.

The EDS elemental map of photoelectrode cross-section (Fig. 3c) shows that the active photocatalytic layer (SnO_2 grains covered by hematite) has a thickness of about 5 μm for the photoanode grown at 60 min precursor deposition. This estimation is confirmed by the data showing the intensity change of Fe signal along a line crossing the photocatalytic layer of the photoelectrode (Fig. 3e). However, the high porosity of ceramics and the presence of large micropores lead to deeper penetration of hematite precursor into ceramics in some places of the substrate (Fig. 3c). This is clearly seen as well in Fig. 3d, showing the C distribution in a cross-section of photoelectrode. The high concentration of carbon is observed mainly on the surface and in a near-surface volume of photoelectrode, while it is negligible deep in the substrate. This shows that the metalorganic precursor of hematite is the main source of carbon detected in the photoelectrode.

The EDS mapping of all photoelectrodes grown onto CuO-Sb_2O_5-SnO_2 ceramics shows that the thickness of the photocatalytic layer is not changed substantially if the deposition time of the hematite precursor is in the range from 10 to 90 min and is close to 5 μm. For the hematite photoelectrodes which were grown onto the Sb_2O_5-SnO_2 ceramic substrates [42], the thickness of the photocatalytic layer was larger, reaching up to 20 μm in some places. However, the Sb_2O_5-SnO_2 ceramic substrate was more porous than the CuO-Sb_2O_5-SnO_2. These data suggest that the depth of precursor penetration into the ceramic substrate is mainly determined by its morphology (porosity and grain size). The CuO-addition results in that CuO-Sb_2O_5-SnO_2 ceramics having higher mechanical strength and density than Sb_2O_5-SnO_2 ceramics, 6.27 g/cm^3 and 5.77 g/cm^3, respectively. However, the electrical conductivity of the CuO-Sb_2O_5-SnO_2 substrate is lower than that of the Sb_2O_5-SnO_2 one, 0.012 and 0.017 S m^{-1}, respectively.

X-ray photoelectron spectroscopy analysis was carried out to analyze the surface chemistry of the hematite photoanodes grown for 90, 60, and 10 min on antimony-doped SnO_2 substrates. The corresponding survey spectra and the comparative Fe2p-, Sn3d-, and O1s-scans recorded for these photoanodes are shown in Fig. 4S (Supplementary Materials). The Fe2p-scans for the photoelectrodes grown for 90, 60, and 10 min have a similar shape shown in Fig.4a. However, the relative intensity of the Fe-signal for the photoelectrodes grown for 10 min is lower than that of those grown for 60 and 90min (Fig.4S b). This is can be explained by the lower hematite content deposited on the photoelectrode surface for 10 min compared to those deposited for 60 and 90min. The Fe-signal for the photoelectrode grown for 60 min contains the $Fe2p_{3/2}$ and $Fe2p_{1/2}$ as main peaks centered at binding energies of about 711 eV and 725 eV, respectively (Fig.4a), which is in accordance with the literature data [56-59]. The $Fe2p_{3/2}$ -signal is accompanied by a satellite peak centered at 719 eV (Fig.4a). This shakeup satellite most likely exists due to the presence of a Fe^{3+} species [57-60]. However, the recorded scan in Figure 4a does not contain evidence of the presence of Fe^{2+}, which should appear as the rise of Fe-signal at 716eV [57]. These data suggest that the concentration of Fe^{2+} species is negligible on the photoelectrode surface.

The Sn-signal for the photoelectrode grown for 60 min contains the Sn $3d_{3/2}$ and Sn $3d_{5/2}$ peaks which are centered at 495.2eV and 487 eV, respectively (Fig.4b). The position of $Sn3d_{5/2}$ peak at 487 eV suggests that the Sn-doping on hematite coating is negligible. Otherwise, this peak should be observed close to 486eV [59, 60].

The O1s and Sb3d signals recorded for the hematite photoelectrodes grown on SnO_2 ceramics doped by Sb are overlapped (Fig. 4c). Both these spectra recorded for the photoelectrodes grown for 60 and 90 min look very similar (curves 1 and 2 in Fig.4c). However, they differ from the spectrum obtained for the photoelectrode grown for 10 min (curve 3 in Fig.4c). The difference is observed at binding energies of about 540 eV and 531 eV (Fig.4c) and, as can be seen in Figure 4d, is related to the presence of the $Sb3d_{3/2}$ and $Sb3d_{5/2}$ – peaks in the spectrum of the photoelectrode grown for 10 min. The $Sb3d_{3/2}$ and $Sb3d_{5/2}$ peaks are centered at binding energies of about 540.5eV and 530.3eV, respectively (Fig.4d). These peaks cannot be considered as a sign of Sb-doping on hematite coating, because they are not observed for the photoelectrodes grown for 60 and 90 min (Fig.4c, curves 1 and 2). Therefore, their origin probably belongs to the ceramic substrate which was not covered totally by hematite for 10 min-deposition.

The deconvolution of the O1s-signal is presented in Figure 4d and three peaks centered at 529.9, 531.2, and 532.3 eV are shown. According to [60], the peak at 529.9 eV is caused by the metal-oxygen bonds, while the 531.2eV and 532.3 eV peaks correspond to the superficial bridging and terminal OH-groups respectively.

Photoelectrochemical characteristics

The values of photocurrent density showed by the hematite photoelectrodes at 1.23 V vs RHE under blue LED light (455 nm, 198 mW/cm^2) in 0.1 M NaOH electrolyte are presented in Fig. 5 as a function of deposition time. The herein reported values of photocurrent density were taken from plots recorded under the permanent LED illumination. The maximum photocurrent (4.79 mA/cm^2) is observed for photoelectrodes grown at the deposition of hematite precursor for 60 min. The correspondent incident photon-to-current efficiency estimated for this photoelectrode at the wavelength of 455 nm is 6.59%. For photoelectrodes prepared at the same condition but with shorter or larger deposition time (10-90 min), the photocurrent density is lower (Fig. 5). Taking note of almost the same thickness of the photocatalytic layer in all photoelectrodes grown at precursor deposition for 10-90 min, the distinct photocurrent values can result from different thicknesses of hematite coating on individual grains. According to literature data, an optical thickness for pure hematite is 45 nm at a wavelength of 400 nm [61], and a diffusion length is around 2–4 nm [62] or even shorter (0.5–1.5 nm [63]). Consequently, the very thin hematite coating on SnO_2 grains which was obtained at a short deposition time (<60 min) is not assured a good light absorption. In turn, the thick hematite films which were grown at large deposition time (>60 min) hamper the hole diffusion to the photoelectrode surface.

The photoelectrodes grown for 60 min have the highest photocurrent response because they possess the most favorable thickness of hematite coating for light absorption and hole diffusion among all obtained photoelectrodes. Their hematite coating on individual grains reaches the thickness (~50 nm) comparable with an optical thickness reported for hematite and, at the same time, is thinner than coatings of other photoelectrodes grown at larger deposition time (> 60 min). This combination assures their good PEC-performance.

The data of linear sweep voltammetry typical for the hematite photoelectrode grown for 60 min and exposing the highest photocurrent (4.79 mA/cm^2 at 1.23 V vs. RHE) are presented in Fig. 6 (curves 1-3). The inset in Fig. 6 shows the photocurrent recorded for the bare substrate (the ceramic substrate not

covered by hematite) under chopped blue LED's light. As seen, the photocurrent for the bare substrate is about 18 μAcm^{-2} at 1.23 V vs RHE that is negligible in comparison with the photocurrent showed by the hematite photoelectrode. This shows that the PEC performances of the reported herein photoelectrodes are related mainly to their hematite coating.

Under chopped blue light (curve 2 in Fig. 6) the photoelectrode shows higher photocurrent (5.2 mA/cm^2 at 1.23 V vs. RHE) than in the case when blue light is kept permanently turned on (curve 3 in Fig. 6). The observed difference in photocurrent values is probably related mostly to the effects of hole accumulation on the hematite surface. This supposition follows from the behavior of photocurrent-time dependency recorded at a fixed potential of 1.23 V vs. RHE under the radiation of the AM1.5G solar simulator (Fig. 7a). As seen in Fig. 7a, the photocurrent under the solar radiation is 0.38 mA/cm^2 at the beginning of the record and then decreases with time for 15 min up to 82.3% of its initial value. However, after this, the photocurrent recovers up to 96.6% of its initial value after the rest under dark conditions for 14 min during which the accumulated charge has been partially dissipated (Fig. 7a). The dark current in the hematite photoelectrode is about 0.0037 mA/cm^2(Fig. 7a). Under the real sun the photocurrent is 0.41 mA/cm^2 at 1.23 V vs RHE (Fig. 7b). In this regard, it is important to point out that these PEC-parameters have been shown by unmodified hematite photoelectrode without any catalyst, and they are nevertheless comparable or higher than one reported for some modified hematite electrodes [37, 64].

Electrochemical impedance measurements

The porous ceramic substrate without hematite film was immersed into 0.1 M NaOH and impedance data recorded from 1000 Hz to 0.01 Hz with amplitude 10 mV at 1.0 V vs. RHE. The porous nature of the ceramics is revealed in a relatively high capacitance. The data conforms approximately to a simple RC equivalent circuit but is modelled here with a transmission line model to allow comparison to the hematite coated electrodes. The transmission line model uses the Bisquert#3 element [65] with a resistor R2 in series to represent contributions from solution resistance. The transmission line (see Figure 8a) has a set of elements R1 (resistivity in the ceramic substrate), a set of elements R3 (interfacial electron transfer resistance), and a set of capacitors (lumped to C_{total} to represent total interfacial capacitance). The key parameters for the bare electrode are R2 = 11.2 Ω and C_{total} = 23.9 mF. The resulting time constant for charging of the interface can be calculated as τ = R2 × C_{total} = 0.27 s. As a result, high frequency information for the hematite films cannot be obtained, but nevertheless clear impedance data for illuminated hematite samples are obtained.

Fig. 8a shows the impedance data represented as Nyquist plot recorded for the hematite photoelectrodes grown at 60 min time of precursor deposition (in 0.1 M NaOH, 10 mV amplitude, LED illuminated at λ = 455 nm, applied potential 1.0 V vs. RHE). These data represent experimental data (black) and their fitting (green) to the equivalent circuit model shown in Fig. 8a. There are three frequency regions: (I) in the high frequency region only the series resistor R2 is detected; (II) in the middle frequency range the porous ceramic is charged up which leads to transmission line behaviour represented by R1 and C; (III) in the low frequency range the hematite photoactivity is detected as a semi-circle with R3 representing charge transfer and C representing the total interfacial capacitance (ceramic and hematite together) [66-69]. Water oxidation is the photo-reaction taking place at the interface of the hematite coating and electrolyte. As seen in Table 1 with the fitting results, all three photoelectrodes grown at 10 min, 60 min, and at 90 min have increases R2 resistors compared to the R2 value for the bare ceramic. This may be linked to hematite reducing the pore size and therefore increasing the impedance between the ceramic and the surrounding solution. Data for the hematite coatings in the transition line model

compare well with the data for bare ceramic substrate. Values for R1 show a slight decrease whereas C_{total} shows an increase linked to the higher active surface area with illuminated hematite. The charge transfer resistor R3 is very high for bare ceramic, bit then decreases with hematite deposition, which is associated with improved oxygen evolution.

Table 1. The fitting results of EIS data for the hematite photoelectrodes (in 0.1 M NaOH, 10 mV amplitude, LED illuminated at λ = 455 nm, applied potential 1.0 V vs. RHE, in brackets fitting error in %).

Photoelectrode	**R1 / Ohm**	**R2 / Ohm**	**R3 / Ohm**	**C_{total} / mF**
#0 (bare ceramic)	26.6 (4%)	11.2 (1%)	8180 (30%)	23.9 (1%)
#1 (10 min)	27 (3%)	29.8 (1%)	94.7 (1%)	39.1 (1%)
#2 (60 min)	14.6 (4%)	28.2 (1%)	45.8 (1%)	41.4 (2%)
#3 (90 min)	15.9 (3%)	25.2 (1%)	47.4 (1%)	37.2 (1%)

The estimation of the flat band potential for the hematite photoanode grown at 60 min deposition were attempted from the Mott-Schottky analysis (without illumination using 10 Hz frequency). The flat band potential is obtained as -0.68 V vs SHE or -0.32 V vs RHE, which agrees with the literature data, which is generally cited in the range from -0.77 V to -0.43 V vs SHE for undoped hematite [69-73]. However, due to the time constant for interfacial charging this value may predominantly reflect the flat band potential for the SnO_2 ceramic substrate [74,75]. Due to these complexities in the presence of the porous substrate combined with porous hematite deposit, calculation of donor concentration data was not attempted.

4. Conclusion

Hematite photoanodes grown by the MO-CVD technique onto CuO-Sb_2O_5-SnO_2 ceramics acting as high-porous and conductive substrate are reported. The presence of hematite in rhombohedral phase is confirmed by XRD analysis. The XPS analysis shows the presence of Fe^{3+} species on the photoelectrode surface and the absence of the Sn-doping on hematite coating. The PEC-performance of the photoelectrodes strongly depends on deposition time of hematite precursor. The highest photocurrent (in 0.1 M NaOH; 4.79 mA/cm^2 at 1.23 V vs RHE under blue light of Thorlabs LED M455L2) is observed in the photoanode grown for 60 min. Under radiation of real sunlight and the solar simulator (AM1.5G, 79.1 mW/cm^2), the photoelectrodes exhibits 0.41 and 0.38 mA/cm^2 at 1.23 V vs RHE, respectively.

The thickness of the photocatalytic layer (SnO_2-grains covered by hematite) does not notably change in the photoelectrodes grown at deposition time varying from 10 to 90 min and remains close to 5 µm. Therefore, it can be concluded that (i) the depth of precursor penetration into the ceramic substrate is mainly determined by ceramics morphology (porosity and grain size); (ii) an alteration in the PEC-performance of the photoelectrodes grown at different deposition time of precursor is related to the different thickness of hematite coating on individual grains. For the photoelectrodes showing the highest photocurrent, this thickness is less than 50 nm.

The good PEC-performance of obtained photoanodes results from their specific architecture: thin Fe_2O_3-coating with the thickness of 50 nm or less is deposited on conductive SnO_2-grains forming the active photoactive layer into the ceramic substrate up to 5 μm depth, while connected SnO_2-grains are forming a conductive path for electrons. This architecture assures favorable conditions for hole diffusion in hematite to the electrolyte and good light harvesting at the same time. The further engineering of ceramic substrates can improve the PEC-performance of such hematite photoelectrodes, the development of which is a promising path to make large-area photoelectrodes for practical application.

Acknowledgements

The authors thank Prof. L. Peter for his help and useful discussion of the EIS-data. This work was supported by the National Science and Technology Council of Mexico (CONACYT), grant # A1-S-20353. FMA acknowledges PRODEP for his Postdoctoral Fellowship to conduct this research.

Conflicts of interest

The authors declare no conflict of interest in this article.

Reference

1. L.M. Peter, Photoelectrochemical Water Splitting. A Status Assessment, Electroanalysis 27 (2015) 864-871.
2. Y.A. Shaban, Electrocatalysts for Photoelectrochemical Water Splitting, in: Inamuddin, R. Boddula, A.M. Asiri (Eds), Methods for Electrocatalysis, Springer International Publishing, 2020, pp 353-374.
3. T. Takata, K. Domen, Particulate photocatalysts for water splitting: recent advances and future prospects, ACS Energy Lett. 4 (2019) 542-547.
4. Y. He, T. Hamann, D. Wang, Thin film photoelectrodes for solar water splitting, Chem Soc Rev 48(2019) 2182-2215.
5. D.K. Lee, D. Lee, M.A. Lumley, K.S. Choi, Progress on ternary oxide-based photoanodes for use in photoelectrochemical cells for solar water splitting, Chem Soc Rev 48(2019) 2126-2157.
6. F.F. Dias, D. Ivanou, F. Santos, J. Azevedo, A. Mendes, Synthesis of host-guest hematite photoelectrodes for solar water splitting, ChemNanoMat 5(2019) 911-920.
7. D.K. Lee, D. Lee, M.A. Lumley, K.S. Choi, Progress on ternary oxide-based photo-anodes for use in photoelectrochemical cells for solar water splitting, Chem. Soc. Rev. 48(2019) 2126–2157.
8. S. Shen, S.A. Lindley, X. Chen, J.Z. Zhang, Hematite heterostructures for photoelectrochemical water splitting: rational materials design and charge carrier dynamics, Energy Environ. Sci. 9(2016) 2744–2775.
9. D.A. Wheeler, G.M. Wang, Y.C. Ling, Y. Li, J.Z. Zhang, Nanostructured hematite: synthesis, characterization, charge carrier dynamics, and photoelectrochemical properties, Energy Environm. Sci. 5(2012) 6682–6702.
10. R. van de Krol, Y. Liang, J. Schoonman, Solar hydrogen production with nanostructured metal oxides, J. Mater. Chem. 18(2008) 2311–2320.
11. S.A. Carminati, A.N. Barbosa, A.L.M. Freitas, F.L. Freire-Jr, F.L. Souza, A.F. Nogueira, Unraveling the role of single layer graphene as overlayer on hematite photoanodes, Journal of Catalysis 379(2019) 109-118.
12. P.Y. Tang, H.B. Xie, C.Ros, L.J.Han, M. Biset-Peiro, Y.M.He, W. Kramer, A. P. Rodriguez, E. Saucedo, J.R. Galan-Mascaros, T. Andreu, J.R. Morante, J. Arbiol, Enhanced photoelectrochemical water splitting of hematite multilayer nanowire photoanodes by tuning the surface state via bottom-up interfacial engineering, Energy& Environ. Sci. 10(2017) 2124-36.
13. J.W. Moir, E.V. Sackville, U. Hintermair, G.A. Ozin, Kinetics versus charge separation: improving the activity of stoichiometric and non-stoichiometric hematite photoanodes using a molecular iridium water oxidation catalyst, J Phys Chem C 120(2016) 12999-3012.
14. A. Tofanello, A. L. M. Freitas, W. M. Carvalho, T. Salminen, T. Niemi, F. L. Souza, Hematite Surface Modification toward Efficient Sunlight-Driven Water Splitting Activity: The Role of Gold Nanoparticle Addition, J. Phys. Chem. C 11(2020) 6171-6179.
15. S. M. Thalluri, L. Bai, C. Lv, Z. Huang, X. Hu, L. Liu, Strategies for Semiconductor/Electrocatalyst Coupling toward Solar-Driven Water Splitting, Adv. Sci. 7(2020), 1902102-33.
16. A. Vilanova, P. Dias, J. Azevedo, M. Wullenkord, C. Spenke, T. Lopes, A. Mendes, Solar water splitting under natural concentrated sunlight using a 200 cm^2 photoelectrochemical-photovoltaic device, Journal of Power Sources 454(2020), 227890-13.
17. A. Vilanova, T. Lopes, A. Mendes, Large-area photoelectrochemical water splitting using a multi-photoelectrode approach, J Power Sources 398(2020) 224-232.
18. A. Tofanello, S. Shen, F. Leandro de Souza, L. Vaysseres, Strategies to improve the photoelectrochemical performance of hematite nanorod-based photoanodes, APL Mater. 8(2020) 040905-12.

19. E. Samuel, B. Joshi, M.-W. Kim, M.T. Swihart, S.S. Yoon, Morphology engineering of photoelectrodes for efficient photoelectrochemical water splitting, Nano Energy 72(2020) 104648-9.
20. Z. Haider, H. W. Yim, H. W. Lee, H. Kim, Surface and bulk modification for advanced electrode design in photoelectrochemical water splitting, Int J Hydrogen Energy 45(2020) 5793-5815.
21. C.S. Tan, K.W. Kemp, M.R. Braun, A.C. Meng, W. Tan, C.E.D. Chidsey, W. Ma, F. Moghadam, P.C. McIntyre, >10% solar-to-hydrogen efficiency unassisted water splitting on ALD-protected silicon heterojunction solar cells, Sustainable Energy Fuels 3(2019) 1490-1500.
22. K. Sivula, F. Le Formal, M. Grätzel, Solar water splitting: progress using hematite (□-Fe_2O_3) photoelectrodes, ChemSusChem 4(2011) 432-441.
23. A. Kay, I. Cesar, M. Grätzel, New benchmark for water photooxidation by nanostructured □-Fe_2O_3 films, J. Amer. Chem. Soc. 128(2006), 15714-8.
24. G. Segev, H. Dotan, K.D. Malviya, A. Kay, M.T. Mayer, M. Grätzel, A. Rothschild, High solar flux concentration water splitting with hematite (□-Fe_2O_3) photoanodes, Adv. Energy Mater. 6(2016) 1500817-10.
25. K.X. Wang, Z. Yu, V. Liu, M.L. Brongersma, T.F. Jaramillo, S. Fan, Nearly total solar absorption in ultrathin nanostructured iron oxide for efficient photoelectrochemical water splitting, ACS Photonics 1(2014), 235-5.
26. P. Perakiatkhajohn, J-H. Yun, H. Chen, M. Lyu, T. Butburee, L. Wang, Stable hematite nanosheet photoanodes for enhanced photoelectrochemical water splitting, Adv Mater 28(2016) 6405-5.
27. Y. Makimizu, N.T. Nguyen, J. Tucek, H.-J. Ahn, J.E. Yoo, M. Poornajar, I. Hwang, S. Kment, P. Schmuki, Activation of a-Fe_2O_3 for Photoelectrochemical Water Splitting Strongly Enhanced by Low Temperature Annealing in Low Oxygen Containing Ambient, Chem. Eur. J. 26(2020) 2685 – 2692.
28. M. Orlandi, A. Mazzi, G. Arban, N. Bazzanella, P. Rudatis, H.B. Caramori, et al. On the effect of Sn-doping in hematite anodes for oxygen evolution, Electrochim Acta 214(2016) 345-8.
29. J.R. McKone, N.S. Lewis, H.B. Gray, Will solar-driven water-splitting devices see the light of day? Chem Mater 26(2014) 407-7.
30. G. Tamirat, J. Rick, A.A. Dubale, W.N. Sub, B.J. Hwang, Using hematite for photoelectrochemical water splitting: a review of current progresses and challenges, Nanoscale Horiz 1(2016) 243-67.
31. J. Joy, J. Mathew, S.C. George, Nanomaterials for photoelectrochemical water splitting- review, Int J Hydrogen Energy 43(2018) 4804-4.
32. K. Maabong, A.G.J. Machatine, B.S. Mwankemwa, A. Braun, D.K. Bora, R. Toth, et al., Nanostructured hematite thin films for photoelectrochemical water splitting, Physica B 535(2018) 67-71.
33. A. Annamalai, R. Sandstrom, E. Gracia-Espino, N. Boulanger, J.F. Boily, I. Muhlbacher, et al. Influence of Sb^{5+} as a double donor on hematite (Fe^{3+}) photoanodes for surface-enhanced photoelectrochemical water oxidation, ACS Appl Mater Interfaces 10(2018) 16467-73.
34. P.Y. Tang, H.B. Xie, C. Ros, L.J. Han, M. Biset-Peiro, Y.M. He, et al., Enhanced photoelectrochemical water splitting of hematite multilayer nanowire photoanodes by tuning the surface state via bottom-up interfacial engineering, Energy Environ Sci 10(2017) 2124-36.
35. C. Li, Z. Luo, T. Wang, J. Gong, Surface, Bulk, and Interface: Rational Design of Hematite Architecture toward Efficient Photo-Electrochemical Water Splitting, Adv. Mater. 30(2018) 1707502-23.
36. F. Francisco, P. Dias, D. Ivanou, F. Santos, J. Azevedo, A. Mendes, Synthesis of Host-Guest Hematite Photoelectrodes for Solar Water Splitting, CHEMNANOMAT 5(2019) 911-920.

37. Z. Wang, X. Lia, C.K. Tan, C. Qian, A.C. Grimsdale, A.Y.Tok, Highly porous SnO_2 nanosheet arrays sandwiched within TiO_2 and CdS quantum dots for efficient photoelectrochemical water splitting, Applied Surface Science 470(2019) 800-806.
38. M. Stefik, M. Cornuz, N. Mathews, T. Hisatomi, S. Mhaisalkar, M. Grätzel, Transparent conduction Nb:SnO_2 for host-guest photoelectrochemistry, Nano Lett 12(2012) 5431-4.
39. A.J. Olaya, T. Omatsu, J.C. Hidalgo-Acosta, J.S. Riva, V.C. Bassetto, N. Gasilova, et al. A self-assembled organic/metal junction for water photo-oxidation. J Am Chem Soc 141(2019) 6765-9.
40. I. Kondofersky, H. Dunn, A. Mueller, B. Mandlmeier, J.M. Feckl, D. Fattakhova-Rohlfing, et al., Electron collection in host-guest nanostructured hematite photoanodes for water splitting: the influence of scaffold doping density, ACS Appl Mater Interfaces 7(2015) 4623-30.
41. A. Mao, G. Y. Hana, J. H. Park, Synthesis and photoelectrochemical cell properties of vertically grown α-Fe_2O_3 nanorod arrays on a gold nanorod substrate, J. Mater. Chem. 20(2010) 2247-2250.
42. A.N. Bondarchuk, I. Corrales-Mendoza, S.A. Tomas, F. Marken, A hematite photoelectrode grown on porous and conductive SnO_2 ceramics for solar-driven water splitting, Int. J Hydrogen Energy 44(2019) 19667-19675.
43. A.N. Bondarchuk, I. Corrales-Mendoza, J.A. Aguilar-Martínez, S.A. Tomás, D.A. Gómez-Caiceros, A. Hernández-Méndez, F. Marken, $BiVO_4$ Photoanode Grown on Porous and Conductive SnO_2 Ceramics for Water Splitting Driven by Solar Energy, Ceramics International 46(2020) 9040–9049.
44. X.Hu, H.Wang, M.Wang, Z. Zang, Interfacial defects passivation using fullerene-polymer mixing layer for planar-structure perovskite solar cells with negligible hysteresis, Solar Energy 206 (2020) 816-825.
45. S. Cao, H. Wang, H. Li, J. Chen, Z. Zang, Critical role of interface contact modulation in realizing low-temperature fabrication of efficient and stable CsPbIBr2 perovskite solar cells, Chemical Engineering Journal 394 (2020) 124903-10.
46. H. Wang, H. Li, S. Cao, M. Wang, J.Chen, Z. Zang, Interface Modulator of Ultrathin Magnesium Oxide for Low-Temperature Processed Inorganic CsPbIBr2 Perovskite Solar Cells with Efficiency Over 11%, Solar RRL 4 (2020) 2000226-10.
47. M. Liu, Y. Zhou, G. Dong, W. Wang, J. Wang, C. Liu, F. Liu, D. Yu, SnO2/Mg combination electron selective transport layer for Si heterojunction solar cells, Solar Energy Materials and Solar Cells 200 (2019) 109996-10.
48. A. Glot, R. Bulpett, A. Ivon, P. Gallegos-Acevedo, Electrical properties of SnO_2 ceramics for low voltage varistors, Physica B: Condensed Matter 457(2015) 108 – 112.
49. D. Clarke, Varistor Ceramics, J. Am. Ceram. 82(1999) 485 – 502.
50. P.R. Bueno, J.A. Varela, E. Longo, SnO_2, ZnO and related polycrystalline compound semiconductors: an overview and review on the voltage-dependent resistance (non-ohmic) feature, J. Eur. Ceram. 28(2008) 505-529.
51. I. Skuratovsky, A. Glot, E. Bartolomeo, E. Traversa, R. Polini, The effect of humidity on the voltage–current characteristic of SnO_2 based ceramic varistor, J. Eur. Ceram. 24(2004) 2597 – 2604.
52. S. Das, V. Jayaraman, SnO2: A comprehensive review on structures and gas sensors, Progress in Materials Science 66 (2014) 112-255.
53. B. Yuliarto, G. Gumilar, N. L. Wulan-Septiani, SnO_2 Nanostructure as Pollutant Gas Sensors: Synthesis, Sensing Performances, and Mechanism, Advances in Materials Science and Engineering 2015(2015) 1-14.
54. I. Corrales-Mendoza, A. Conde-Gallardo, Growth of NdFeAsO films by a combination of metal–organic chemical vapor deposition and Arsenic Diffusion Processes, IEEE Transactions on Applied Superconductivity 24(2014) 111-116.
55. Z. Chen, T. G. Deutsch, H. N. Dinh, K. Domen, K. Emery, A. J. Forman, N. Gaillard, R. Garland, C. Heske, T. F. Jaramillo, A. Kleiman-Shwarsctein, E. Miller, K. Takanabe, J. A. Turner, Efficiency

Definitions in the Field of PEC, in: Z. Chen, H. N. Dinh, E. Miller (Eds.), Photoelectrochemical Water Splitting, SpringerBriefs in Energy, Springer, New York, 2013, pp. 7-16.
56. S. K. Sarma, R. Mohan, A. Shukla, Structural, opto-electronic and photoelectrochemical properties of tin doped hematite nanoparticles for water splitting, Materials Science in Semiconductor Processing 108 (2020) 104873-10.
57. Y. Ling, G. Wang, J. Reddy, C. Wang, J. Z. Zhang, Y. Li, The Influence of Oxygen Content on the Thermal Activation of Hematite Nanowires, Angew Chem. Int. Ed. 51 (2012) 4074 –4079.
58. A. Subramanian, E. Gracia-Espino, A. Annamalai, H. H. Lee, S. Y. Lee, S. H. Choi, J. Jang, Effect of Tetravalent Dopants on Hematite Nanostructure for Enhanced Photoelectrochemical Water Splitting, Applied Surface Science 427 (2018) 1203–1212.
59. L. Xi, S.Y. Chiam, W. F. Mak, P. D. Tran, J. Barber, S. C. J. Loo, L. H. Wong, A novel strategy for surface treatment on hematite photoanode for efficient water oxidation, Chem. Sci. 4 (2013) 164-169.
60. A. Annamalai, R. Sandström, E. Gracia-Espino, N. Boulanger, J.-F. Boily, I. Mühlbacher, A. Shchukarev, T. Wågberg, Influence of Sb^{5+} as a Double Donor on Hematite (Fe^{3+}) Photoanodes for Surface-Enhanced Photoelectrochemical Water Oxidation, ACS Appl. Mater. Interfaces 10 (2018) 16467–16473.
61. L.A. Marusak, R. Messier, W.B. White, Optical absorption spectrum of hematite, α-Fe_2O_3, near IR to near UV, J. Phys. Chem. Solids 41(1980) 981–984.
62. J.H. Kennedy, K.W. Frese, Photooxidation of Water at α-Fe_2O_3 Electrodes, J. Electrochem. Soc. 125(1978) 709–714.
63. F. LeFormal, K. Sivula, M. Grätzel, The Transient Photocurrent and Photovoltage Behavior of a Hematite Photoanode under Working Conditions and the Influence of Surface Treatments, J. Phys. Chem. C 116(2012) 26707–26720.
64. C.V. Reddy, I.N. Reddy, B. Akkinepally, K.R. Reddy, J. Shim, Synthesis and photoelectrochemical water oxidation of (Y, Cu) codoped α-Fe_2O_3 nanostructure photoanode, Journal of Alloys and Compounds 814(2020) 152349-8.
65. (a)J. Bisquert, G. Garcia-Belmonte, F. Fabregat-Santiago, A. Compte, Anomalous transport effects in the impedance of porous film electrodes, Electrochem. Commun. 1(1999) 429-435. (b) J. Biquert, Influence of the boundaries in the impedance of porous film electrodes, Phys. Chem. Chem. Phys. 2(2000) 4185-4192.
66. T. Lopes, L. Andrade, F. Le Formal, M. Grätzel, K. Sivula, A. Mendes, Hematite photoelectrodes for water splitting: evaluation of the role of film thickness by impedance spectroscopy, Phys. Chem. Chem. Phys. 16 (2014) 16515-16523.
67. B. Klahr, S. Gimenez, F. Fabregat-Santiago, T. Hamann, J. Bisquert, Water Oxidation at Hematite Photoelectrodes: The Role of Surface States, J. Am. Chem. Soc. 134(2012) 4294– 4302.
68. H. Naatz, R. Hoffmann, A. Hartwig, F. La Mantia, S. Pokhrel, L. Mädler, Determination of the Flat Band Potential of Nanoparticles in Porous Electrodes by Blocking the Substrate-Electrolyte Contact, J. Phys. Chem. C 5(2018) 2796-2805.
69. A. Hankin, F.E. Bedoya-Lora, J. C. Alexander, A. Regoutz, G. H. Kelsall, Flat band potential determination: avoiding the Pitfalls, J. Mater. Chem. A 7(2019) 26162–26176.
70. J.A. Glasscock, P. R. F. Barnes, I. C. Plumb, N. Savvides, Enhancement of Photoelectrochemical Hydrogen Production from Hematite Thin Films by the Introduction of Ti and Si, J. Phys. Chem. C 44(2007) 16477–16488.
71. J.H. Kennedy, K.W. Frese-Jr., Photoactivity of doped α-Fe_2O_3 electrodes, J. Electrochem. Soc. 125(1978) 723-735.

72. R.K. Quinn, R.D. Nasby, R.J. Baughman, Photoassisted electrolysis of water using single crystal α-Fe_2O_3 anodes, Mater. Res. Bull. 11(1976) 1011-1017.
73. S.U. M. Khan, J. Akikusa, Photoelectrochemical Splitting of Water at Nanocrystalline n-Fe_2O_3 Thin-Film Electrodes, J. Phys. Chem. B 34(1999) 7184–7189.
74. J. Bandara, R.A.S.S. Ranasinghe, The effect of MgO coating on photocatalytic activity of SnO_2 for the degradation of chlorophenol and textile colorants; the correlation between the photocatalytic activity and the negative shift of flatband potential of SnO_2, Appl. Catal. A Gen. 319(2007) 58-63.
75. G. Boschloo, D. Fitzmaurice, Spectroelectrochemistry of highly doped nanostructured tin dioxide electrodes, J. Phys. Chem. B 16(1999) 3093–3098.

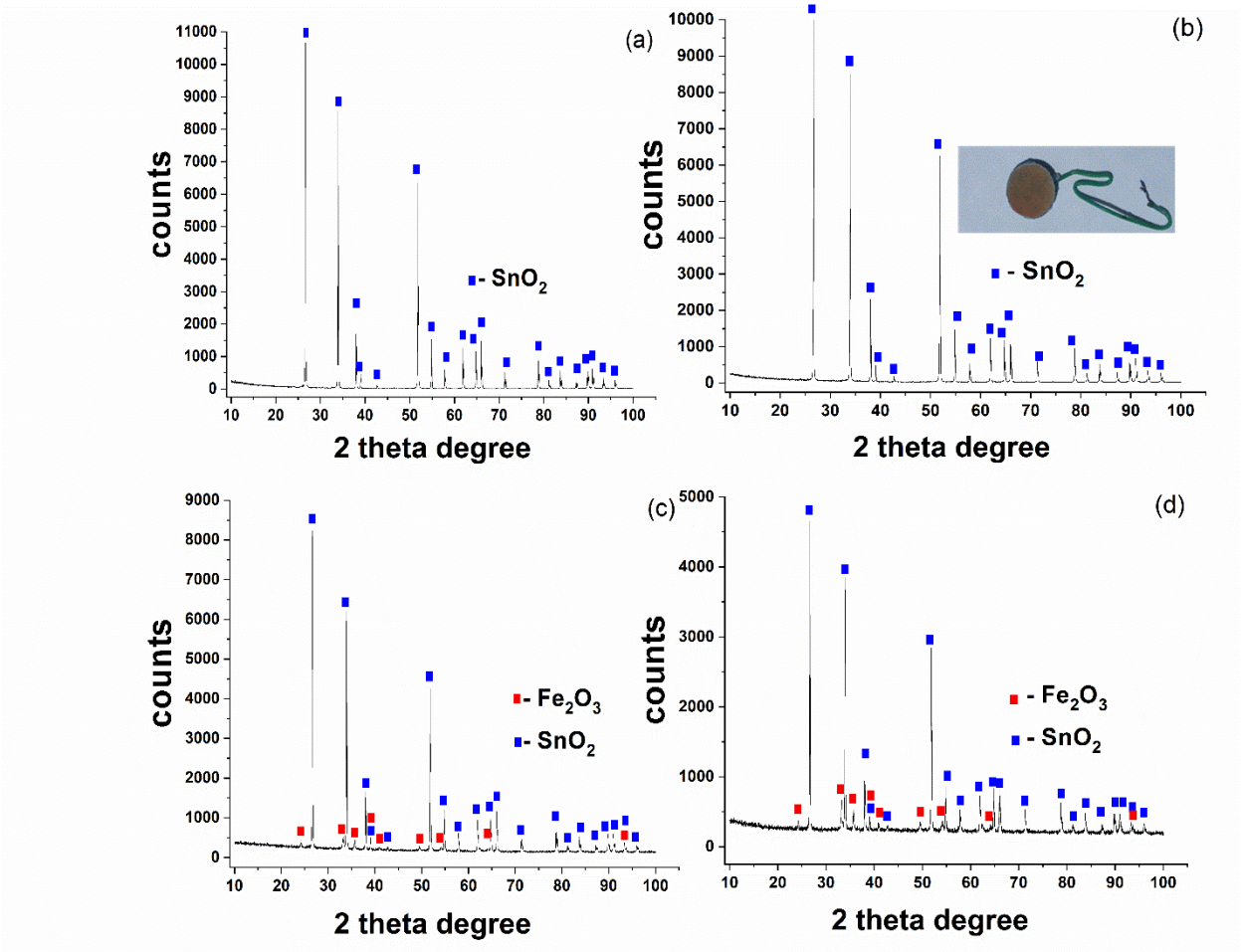

Fig.1. XRD patterns for the Fe_2O_3 photoelectrodes grown on CuO-Sb_2O_5-SnO_2 ceramic substrate at different deposition time of precursor: (a) bare substrate; (b)10 min; (c) 60min; (d)90min. The inset presents the image of the front side of photoelectrode grown for 10-min.

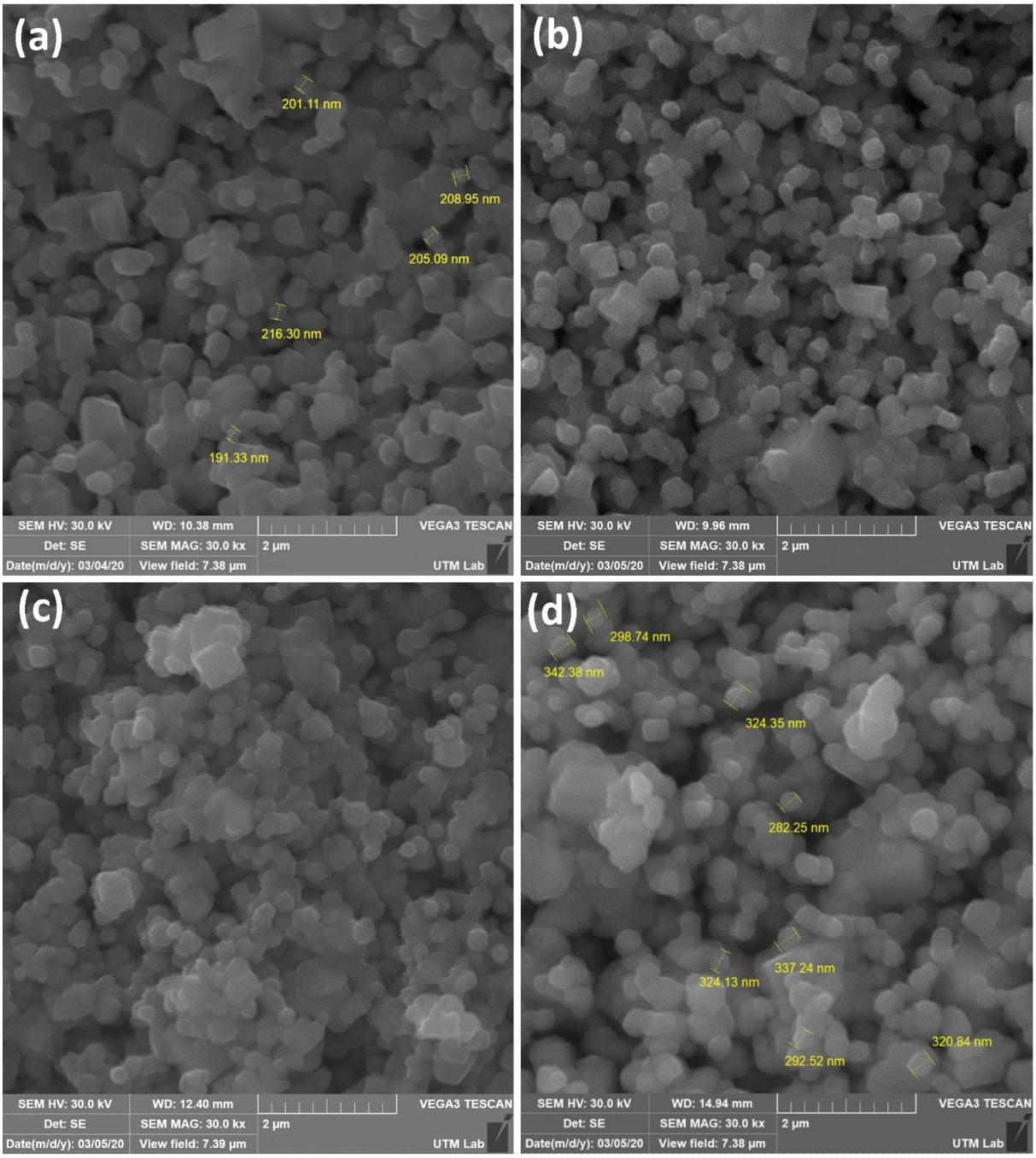

Fig. 2. SEM micrographs for (a) bare CuO-Sb_2O_5-SnO_2 ceramics and (b-d) ceramics with hematite coating grown at different deposition time: (b) 10min, (c) 60min, and (d) 90min.

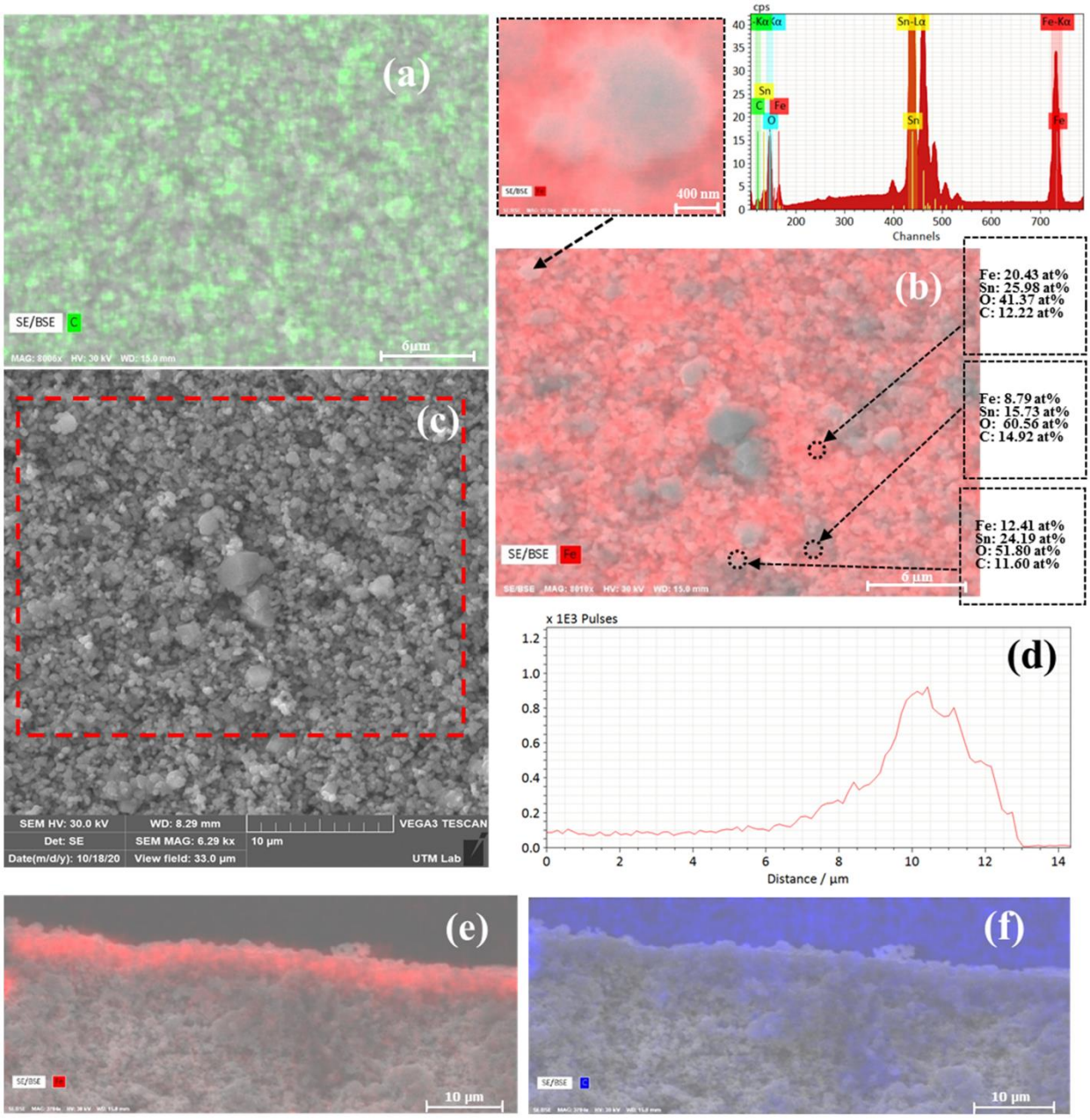

Fig. 3. EDS data for the hematite photoelectrode grown for 60min: (a),(b) the front side in the area shown in (c); (d), (e),(f) — in cross-section where (e) is the intensity change of Fe -signal along a line crossing the photocatalytic layer.

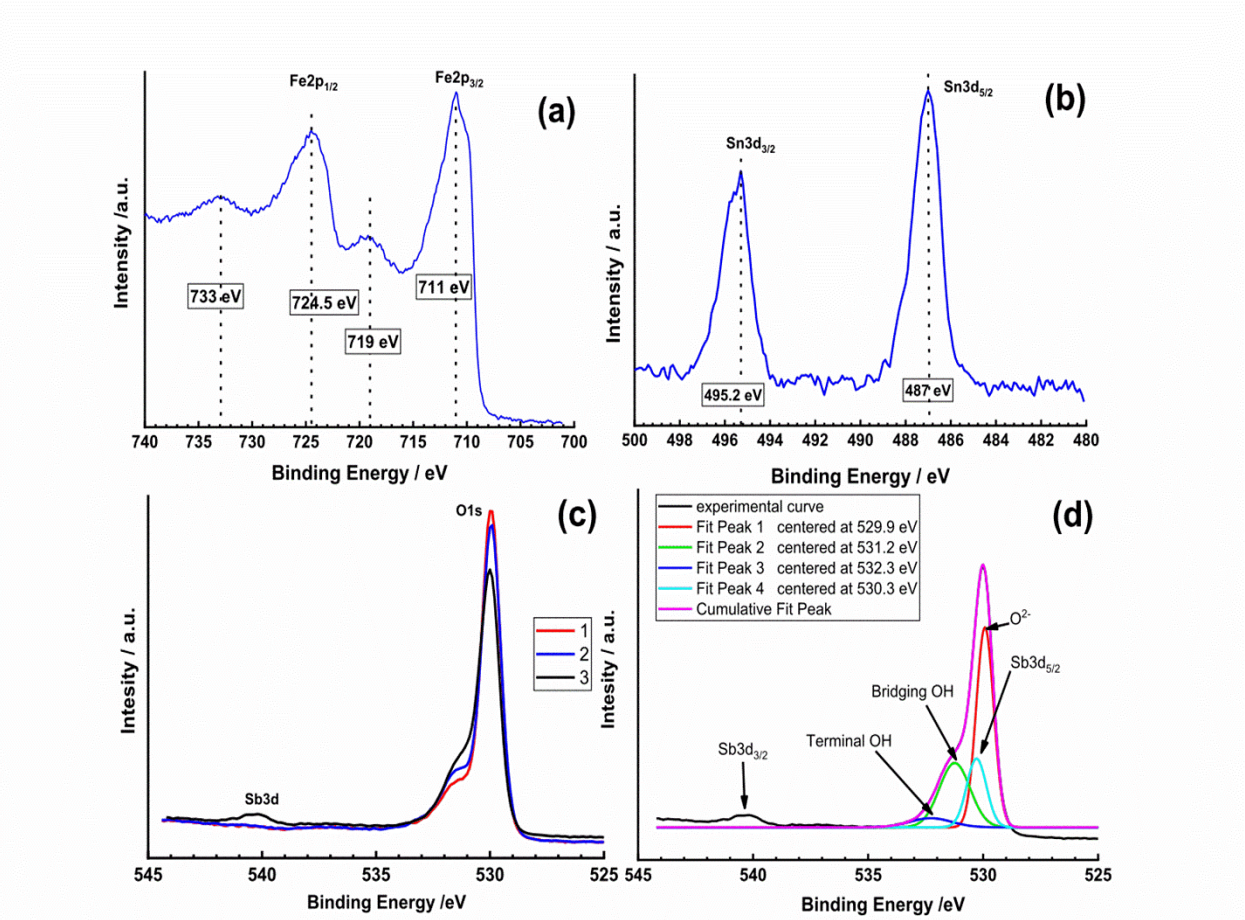

Fig.4. XPS spectra of (a)Fe2p-, (b) Sn3d-, and (c),(d) O1s-scans rerecorded on surface of the hematite photoelectrodes. The signals in (a), (b), and the fitted O1s-signal in (d) were obtained for the photoelectrode grown for 60min. The O1s-scans showed in (c) were recorded for the photoelectrodes grown for 90 min (curve 1), 60 min(curve 2), and 10 min (curve 3).

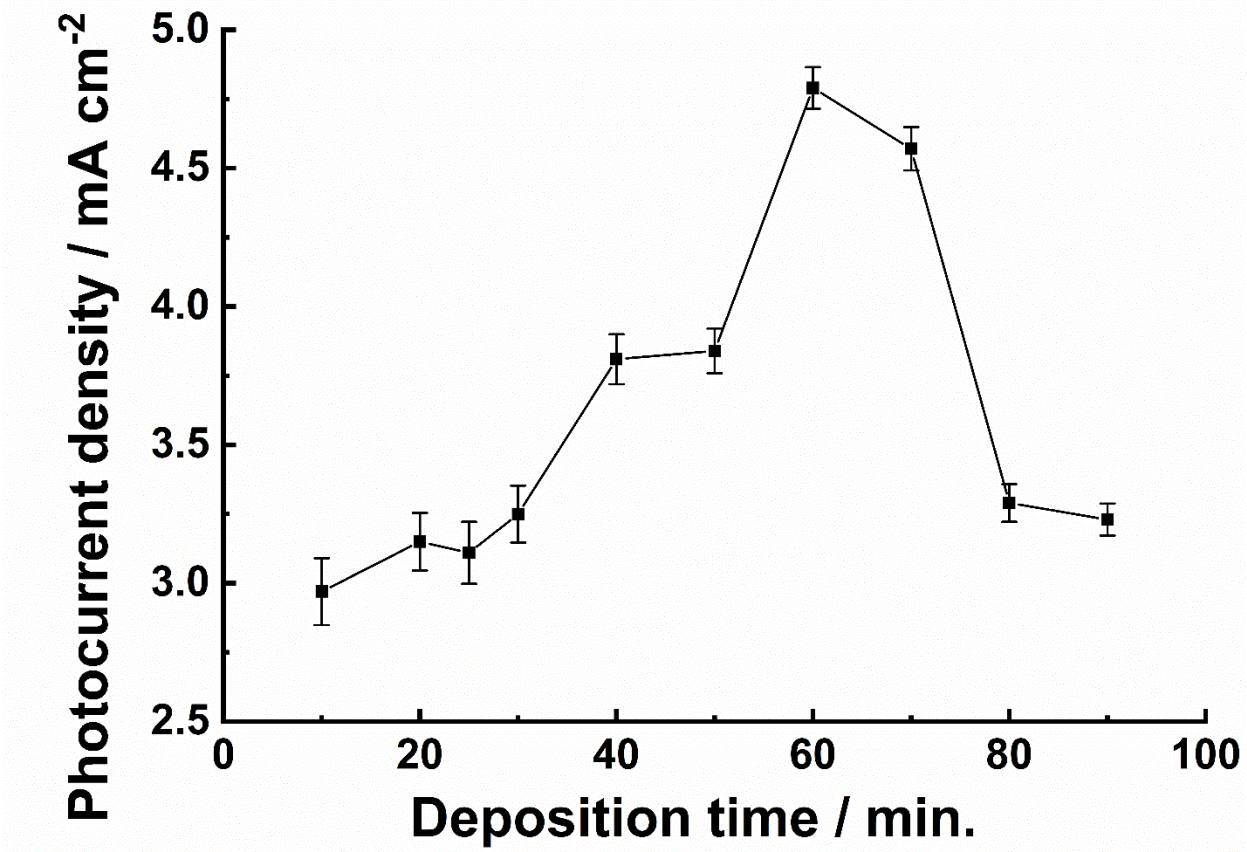

Fig.5. The photocurrent density registered at 1.23V vs. RHE under blue LED's light in 0.1 M NaOH electrolyte for hematite photoelectrodes grown at different deposition time of precursor. The bars show the deviation of photocurrent values from their average values obtained for photoelectrodes grown at the same deposition time.

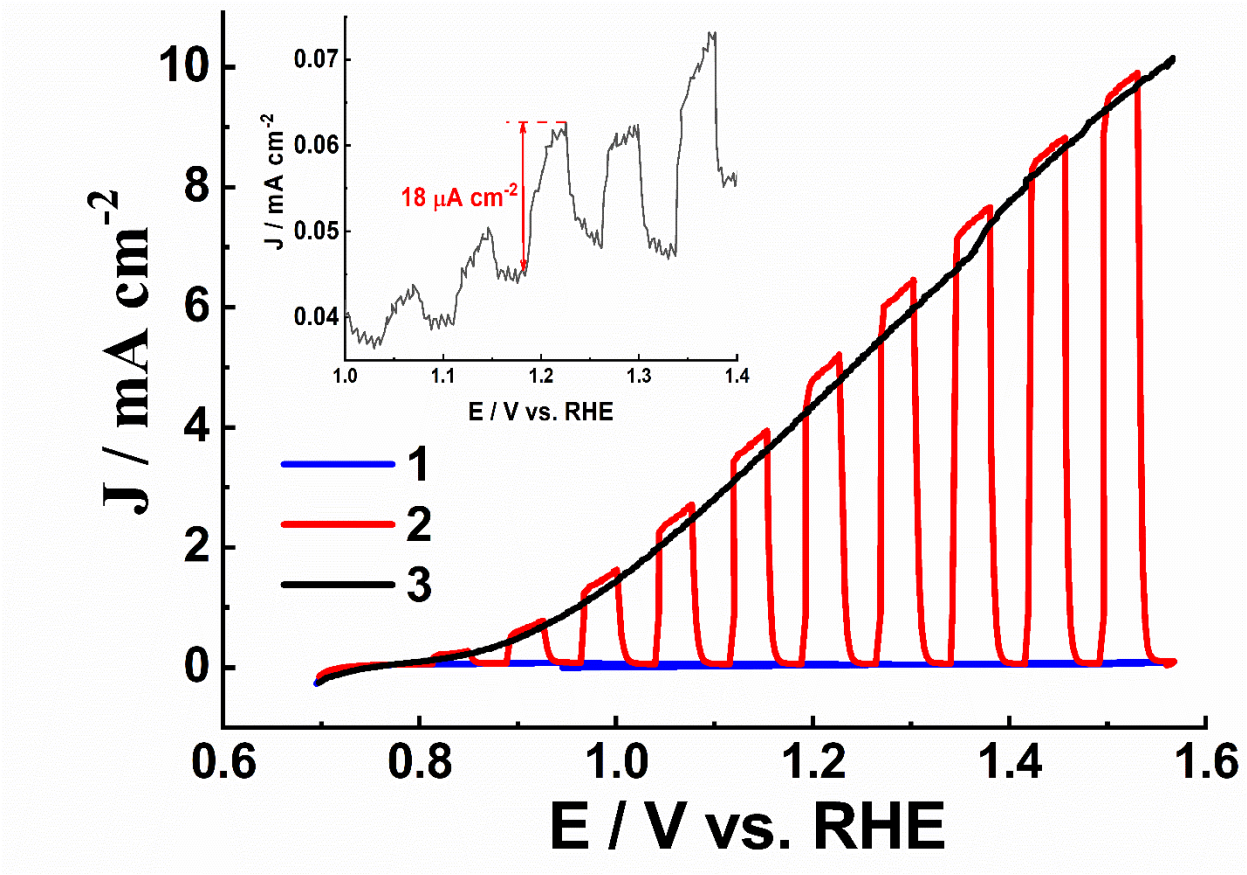

Fig.6 Cyclic voltammetry (scan rate 2.5 mV s^{-1}; 0.1 M NaOH electrolyte) for a hematite photoelectrode grown for 60min. Curves were recorded at the increase of potential under dark condition (curve 1), under chopped blue LED's light (curve 2), and when blue light is kept permanently turned on (curve 3). The inset shows the photocurrent for bare ceramic substrate recorded at the increase of potential under chopped blue LED's light.

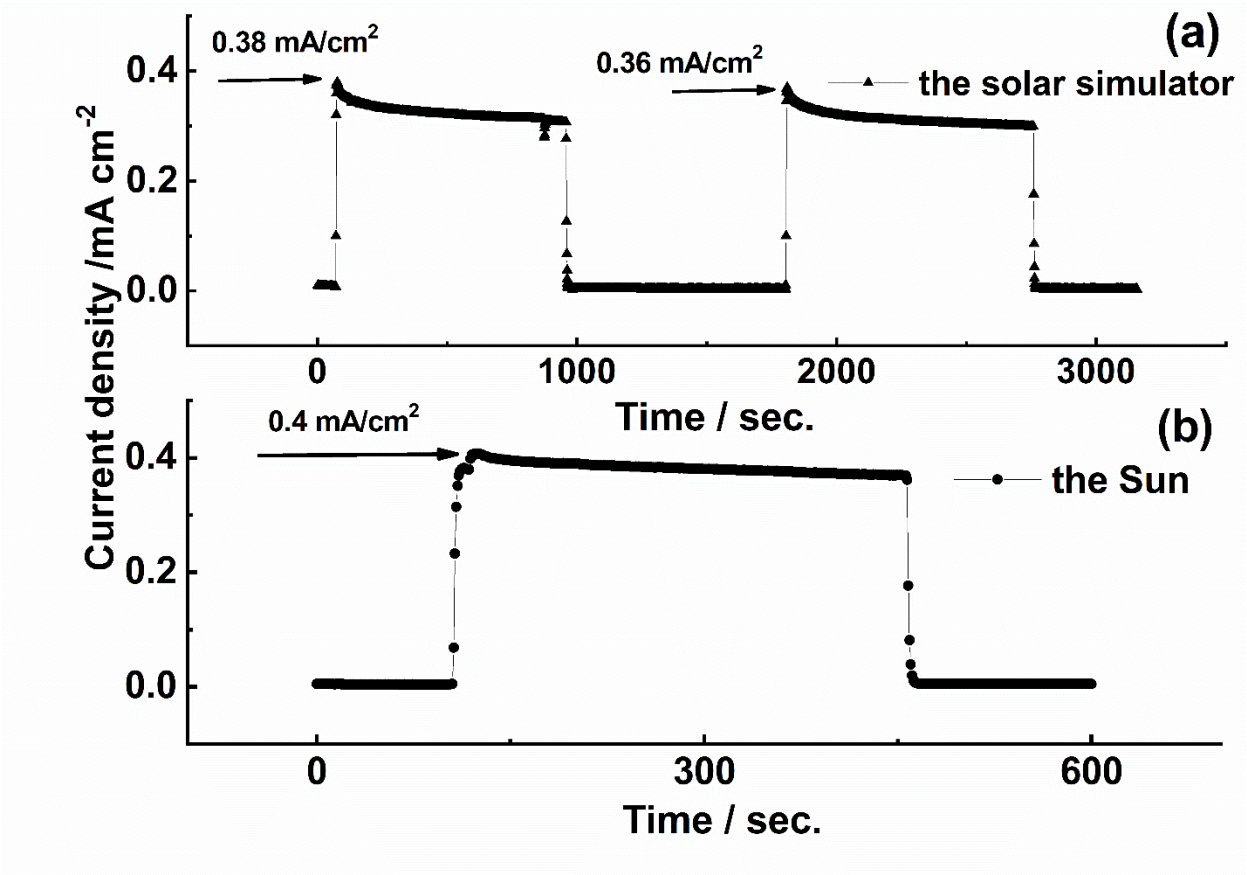

Fig. 7. Photocurrent-time dependency recorded at 1.23V vs RHE in 0.1 M NaOH electrolyte for the photoelectrode grown for 60 min under (a) the AM1.5G- and (b) the Sun- radiation alternating with dark condition.

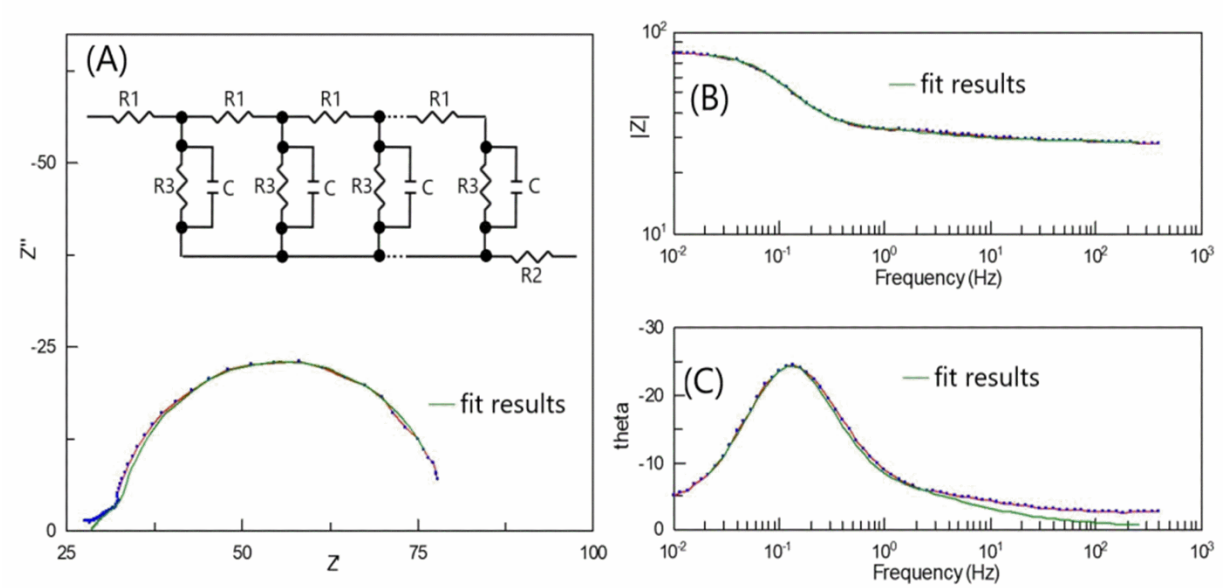

Fig. 8. Photoelectrochemical impedance data recorded at 1.23V vs RHE in 0.1 M NaOH electrolyte for the photoelectrode grown for 60 min under LED illumination. (A) Nyquist plot and equivalent circuit (transmission line based on model Bisquert#3); (B, C) Bode plots. The experimental data are presented by blue dots with a red line and fitting results— by a green line.